The CLAS12 Beamline and its Performance

N. Baltzell[a], V.D. Burkert[a], J. Carvajal[f], N. Dashyan[b], R. De Vita[c], L. Elouadrhiri[a], G. Kharashvili[a], A. Kim[d], R. Paremuzyan[e], B.A. Raue[f], Y.G. Sharabian[a], S. Stepanyan[a], M. Tiefenback[a], M. Ungaro[a], K. Wild[f]

[a]*Thomas Jefferson National Accelerator Facility, Newport News, Virginia 23606*
[b]*A. Alikhanian National Laboratory, 375036 Yerevan, Armenia*
[c]*INFN, Sezione di Genova, Via Dodecaneso 33, I-16146, Genova, Italy*
[d]*University of Connecticut, Storrs, CT 06269-3046*
[e]*University of New Hampshire, Department of Physics, Durham, NH 03824*
[f]*Florida International University, Miami, FL 33199*

Abstract

This paper describes the Hall B beamline and its performance during the first year of data-taking operation using the CLAS12 detector. We review the beamline instrumentation used to measure and monitor the beam. This instrumentation led to excellent beam quality for energies ranging from 2.2 to 10.6 GeV at the design luminosity of 10^{35} cm^{-2}s^{-1}. The instrumentation includes a Møller polarimeter, which can typically measure the beam polarization to an absolute precision of ∼2.5%.

Keywords: electron beam, collimator, heavy photon, electromagnetic calorimeter, polarimeter

1. Introduction

The physics program for CLAS12 in Hall B at Jefferson Lab requires the use of electron beams of various energies and currents that impinge upon targets ranging from liquid hydrogen to lead. A significant part of the physics program includes running with polarized targets that require a rastered beam on the target. In order to extract experimental observables, accurate measurements of the beam charge and polarization are required. Also, for safe and efficient operation of a large, open acceptance spectrometer, proper shielding and a stable beam with a small lateral size and minimal beam halo are necessary.

The Hall B beamline is designed to satisfy the experimental requirements and to provide the necessary controls and monitoring of the electron beam properties for safe and efficient operation of CLAS12. The key set of parameters required by experiments with CLAS12 is listed in Table 1. The main challenges for the beamline setup are the open acceptance of CLAS12 and the close proximity of various sensitive detectors to the target and beam. Such challenges were successfully overcome in Hall B in the past for CLAS experiments [1] and the Heavy Photon Search (HPS) experiment [2].

A few key modifications to the beamline used during the lower-energy run of the HPS experiment [3] have been introduced in order to establish high-quality physics beams in Hall B and run CLAS12 at the design luminosity of 10^{35} cm^{-2}s^{-1}. Additions to the beamline for high-energy running of CLAS12 include a new intermediate beam dump upstream of the hall, a cryogenic target system, shielding downstream of the target to protect the CLAS12 detectors from electromagnetic backgrounds, and the Møller polarimeter for beam polarization measurements.

Parameter	Requirement	Unit
Beam energies	≤ 11	GeV
Beam currents	< 500	nA
Current instability	∼ 10	%
Accuracy of current measurement	∼ 1	%
Beam widths (σ_x, σ_y)	< 300	μm
Position stability	< 200	μm
Divergence	< 100	μrad
Beam halo (> 5σ)	$< 10^{-4}$	
Beam polarization	>80	%
Accuracy of polarization measurement	< 3	%

Table 1: Nominal required Hall B beam parameters.

In this paper we discuss the design of the Hall B

beamline for CLAS12 and its performance during the 2018 experimental run. We review the beamline instrumentation used to measure and monitor the beam parameters and to protect the CLAS12 detectors against errant beam motion. As will be demonstrated, excellent quality and stability of the CEBAF beams, coupled with the Hall B beamline protection systems, allowed operation of the CLAS12 detector at the design luminosity.

2. Hall B Beamline Design

The Hall B beamline is divided into two segments, the so-called "2C" line from the Beam Switch Yard (BSY) following beam extraction from the CEBAF accelerator to Hall B, and the "2H" line from the upstream end of the experimental hall to the beam dump in the downstream tunnel. The beamline upstream of CLAS12 is furnished with a number of quadrupoles, corrector dipoles, and beam diagnostic tools, grouped into sections. Accelerator operators have exclusive control of these devices and use this instrumentation to tune and deliver the beam to the CLAS12 target located approximately at the geometrical center of the hall. In addition to the devices used by accelerator operations, there are several beam position, current, polarization, and halo monitors that are controlled and monitored by the Hall B shift personnel.

For high-energy operation of CLAS12, the 2C beamline as described in Ref. [3] was modified to include the Møller polarimeter located in the upstream tunnel of the hall and an intermediate beam dump just upstream of the hall. Additionally, the 2H beamline (see Fig. 1) now includes a cryogenic target and a tungsten shield downstream of the target inside the CLAS12 torus magnet bore. The Møller polarimeter is used to periodically measure the longitudinal beam polarization and is discussed in more detail in Section 4. The other components are discussed in the following subsections.

2.1. Intermediate Beam Dump Before CLAS12

In order to prevent radiation damage to the sensitive detectors during the initial beam tune, or when errant beam may be sent to the hall, or during the beam polarization measurements with the Møller polarimeter, the beam has to be terminated upstream of CLAS12. For these operations the Hall B tagger dipole magnet is used to deflect the primary beam and secondary scattering products. During low-energy operations, the tagger dipole directs the beam into the tagger beam dump in the hall floor upstream of the CLAS12 spectrometer. The highest energy beam that can be directed to this dump is limited to 6.2 GeV by the maximum field of the tagger dipole, 1.76 T [4]. At higher energies, several options for the intermediate beam dump were considered during the design stage with the optimal solution being to dump the beam inside the bore of the tagger magnet yoke. The design of the intermediate dump was based on full FLUKA [5] simulations and on thermal finite-element analysis. The two main parameters that were studied were the radiation levels at the location of the CLAS12 tracking detectors and the temperature rise in the magnet yoke when up to 10 nA of continuous wave (CW) electron beam is dumped on the yoke.

The FLUKA simulations were used to determine background radiation levels at the tracking detectors for different configurations of the dump and compared with radiation levels from various targets and beam currents at the design luminosity. It was found that acceptable background radiation levels from the dump occur when the beam is steered into the yoke at approximately 33 cm from the upstream entrance to the tagger magnet bore, as shown in Fig. 2. This is done by setting the tagger magnetic field to be $I(\mathrm{A}) = 43.491 \times E(\mathrm{GeV}) - 0.076$, where I and E are the tagger power supply current and the beam energy, respectively.

The FLUKA simulations were also used to guide the design of the shielding around and just downstream of the tagger magnet yoke. The shielding includes lead, borated polyethylene, and concrete blocks. Figure 3 shows the 1-MeV neutron equivalent fluency for the background from the dump and for various beam/target configurations as a function of the position along the beamline. In the graph, the yoke dump position is at approximately -900 cm and the CLAS12 target is at ~400 cm. The figure shows that at the location of the CLAS12 target, the designed shielding configuration (filled black points) results in radiation levels from the yoke comparable to levels for running on a carbon target at the full design luminosity.

To assess the temperature increase in the yoke, a thermal finite-element analysis was set up using ANSYS Workbench v18 [6]. A simplified CAD model of the yoke was imported and modified to include a cylindrical heat load representing the beam. The heating profile from the deposition of 1 kW of power in a cylinder of one Moliere radius (r=1.7 cm) and 10 radiation lengths (17 cm) of iron was calculated. Conservatively, adiabatic boundary conditions were applied to the outer surfaces of the yoke. The model was solved as a transient thermal analysis with 100 time points over 3600 seconds. At the dump location, the temperature was found to initially increase rapidly and then stabilized to a maximum temperature increase of $\Delta T = 54^{\circ}\mathrm{C}$ as the heat

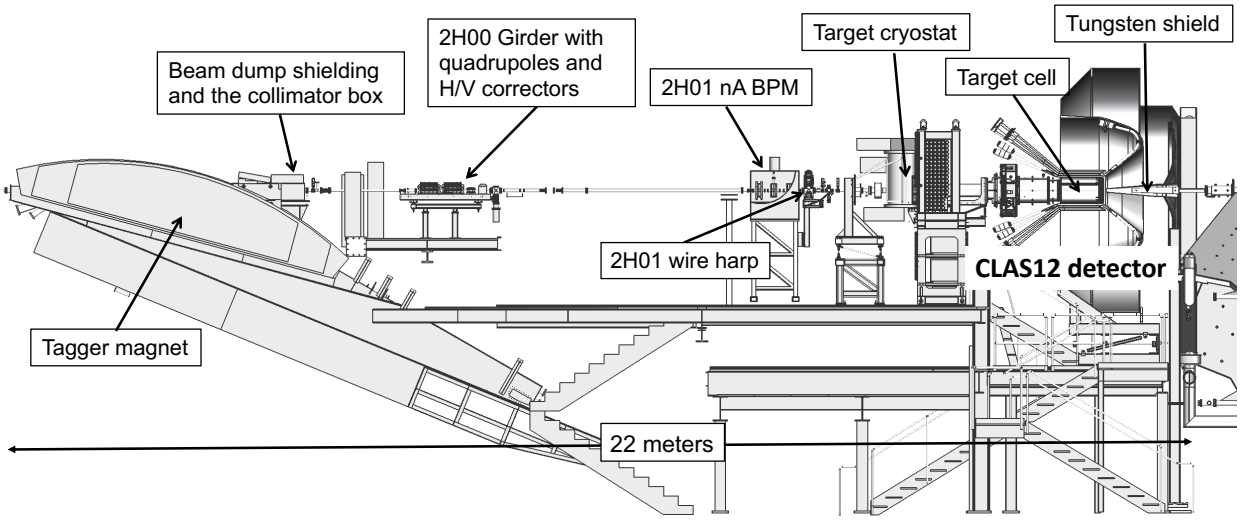

Figure 1: Beamline in Hall B showing beamline elements upstream of the CLAS12 target, cryotarget, CLAS12 Central Detector, and the tungsten shield downstream of the scattering chamber.

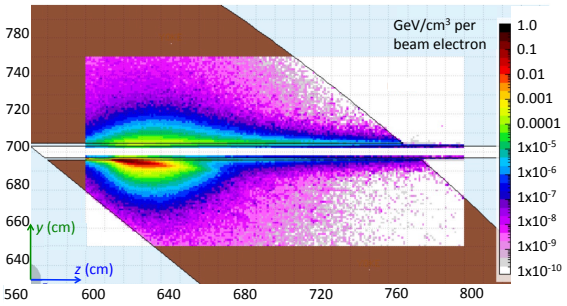

Figure 2: Distribution of energy in the yoke of the tagger dipole magnet from dumping a 10 nA, 11 GeV beam on the yoke at ~33 cm from the upstream entrance to the bore of the tagger magnet. The horizontal and vertical scales are distances in cm and energy deposition (in GeV/cm^3) as indicated by the color scale. The brown region indicates the cross section of the tagger yoke.

dissipates throughout the yoke volume (see Fig. 4). Due to the very large volume and heat capacity of the yoke, the temperature is not expected to rise much higher even for longer beam application times.

2.2. *Cryogenic Target*

Hall B experiments are grouped into running periods according to beam energy and targets. So far two types of cryogenic targets have been used for experiments; liquid hydrogen (LH_2) and liquid deuterium (LD_2). The Hall B cryotarget system from the 6 GeV era [1] has been modified for CLAS12 operations. The current target cell is a 50-mm long Kapton cone with 23.66 mm and 15.08 mm upstream and downstream diameters, respectively. The entrance and exit windows for the beam are 30-μm-thick aluminum. The typical target density is 71 mg/cm^3 for LH_2 and 169 mg/cm^3 for LD_2. The cryo-liquids are sub-cooled to reduce the density variations and prevent boiling and the formation of bubbles. Figure 5 shows the design rendering of the target cell inside the scattering chamber. The scattering chamber is made of Rohacell XT110 foam (density ρ = 0.110 g/cm^3) and is ~45 cm long with a 100 mm outer diameter such that it fits within the CLAS12 Silicon Vertex Tracker (SVT) [8] and provides a minimal material thickness for scattered particles from the target to the CLAS12 detectors.

A beam halo monitor is integrated within the target cell. This device consists of a 40-mm-long glass cylinder with inner and outer diameters of 10 mm and

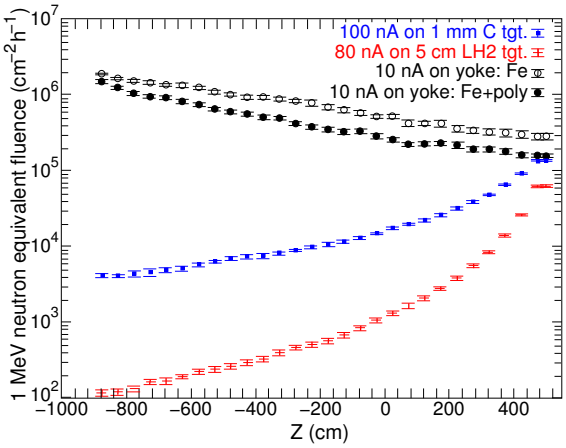

Figure 3: FLUKA simulation of radiation levels in the hall from dumping a 10 nA, 11 GeV beam on the tagger magnet yoke compared to the radiation levels from nominal running on hydrogen and carbon targets. The 1-MeV neutron equivalent fluency as a function of position along the beamline for yoke shielding with iron only (open circles) and with iron and borated polyethylene (filled circles), and for two target configurations, 1 mm carbon (filled squares) and 5 cm liquid hydrogen (crosses).

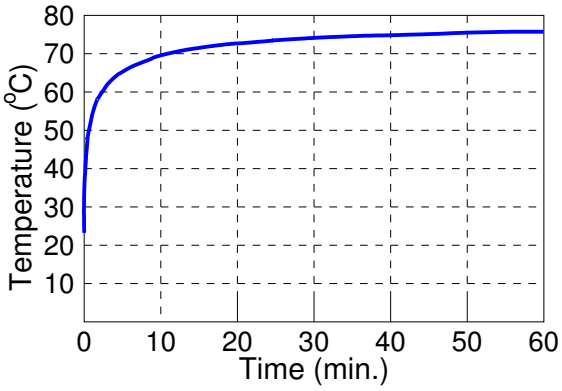

Figure 4: The heat distribution after 60 minutes of beam exposure at the upstream dump location. The highest temperature in the yoke is at the region of impact and is 76°C assuming an initial uniform temperature of 22°C.

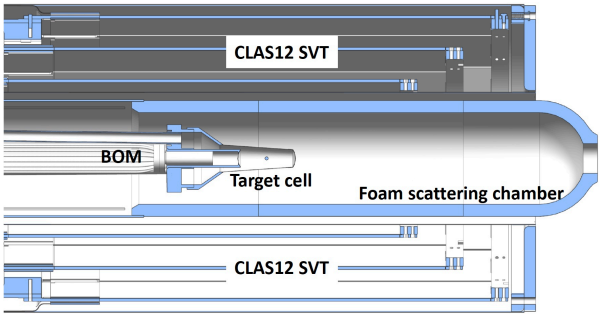

Figure 5: Sketch of the cryogenic target showing the target cell, beam offset monitor, and scattering chamber with associated plumbing and structural supports.

12 mm, respectively, mounted directly on the upstream window of the target cell with its axis parallel to the beamline and with 16 optical fibers attached to the upstream perimeter of the cylinder. Light generated in the cylinder from interactions of the beam halo or from back-scattered secondaries is read out with a multi-anode photomultiplier tube (PMT). The device, called the beam-offset monitor (BOM), is used to monitor the beam position at the target (see discussion below).

The scattering chamber extends downstream of the Central Detector. There is a 50-μm-thick aluminum window on the downstream end of the scattering chamber that closes the upstream vacuum beamline (from the accelerator to the CLAS12 target). The downstream vacuum beamline starts after a 60-cm-long air gap after the scattering chamber and ends at the beam dump.

In addition to the cryogenic targets mentioned above and already used in two experiments (LH_2 and LD_2), there will be experiments that will use nuclear targets in the form of thin foils and experiments with polarized targets. The nuclear target assembly is similar to the cryogenic target cell except that various target foils will be inside the cell instead of a liquid. The cryotarget supply lines will be used to flow helium gas through the cell to dissipate heat in the foils from the beam. Two types of polarized targets will be used for CLAS12 experiments [7]; dynamically (longitudinally) polarized ammonia (NH_3) and deuterated ammonia (ND_3), and a polarized solid HD target in a frozen spin mode.

2.3. *Shielding Downstream of the Target*

Special care was taken to protect the CLAS12 detectors from beam-induced background radiation. The main sources of the background are Møller scattering and small-angle electron scattering along with electromagnetic processes such as bremsstrahlung and pair production. These interactions produce photons, electrons, and positrons that can flood the tracking detectors. GEANT4 simulations of CLAS12 have been used to study backgrounds and design appropriate shielding to reduce the levels of background radiation [9]. The shielding design takes advantage of the 5-T longitudinal magnetic field around the target that is generated by the Central Detector superconducting solenoid magnet. This strong longitudinal magnetic field causes low-energy particles to spiral forward and away from the detectors and into the shielding far downstream of the tar-

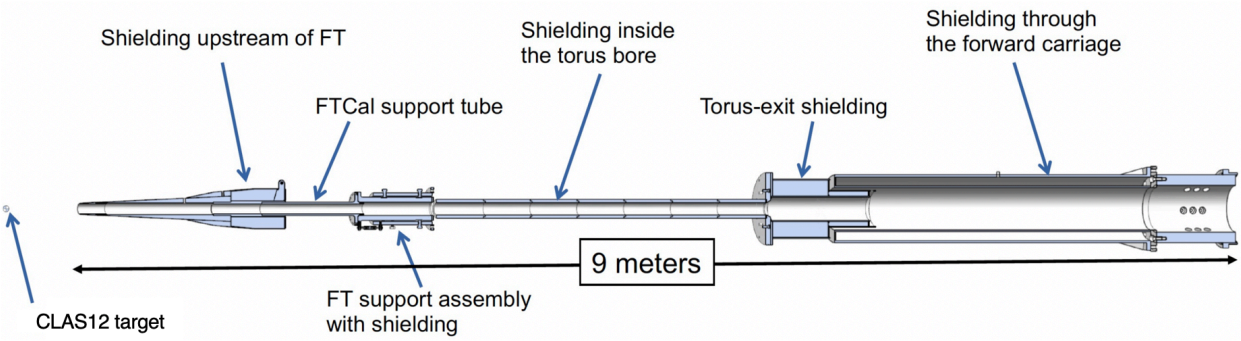

Figure 6: Tungsten shielding downstream of the target, through the torus magnet bore.

get. The heavy shielding materials (lead and tungsten) contain the background and either absorb it or guide the flux of particles out of the downstream end of CLAS12 without interacting in the detectors.

Experiments in CLAS12 will run with or without the Forward Tagger (FT) [10] in use. These two different detector configurations require two different shielding configurations. Figure 6 shows the configuration when the FT is not used (called FT-OFF). The shielding starts with a tungsten cone with a 5-cm diameter hole at the center for the beam. When the FT is in use (called FT-ON), the tungsten cone is mounted directly to the FT central support, which is also made from tungsten. In the latter case, the angular acceptance of particles scattered from the target starts at $\sim 2^\circ$. For the FT-OFF configuration, a large diameter lead cylinder is inserted between the FT central support (after removing the FT tracker) and the tungsten cone, thus moving the tip closer to the target. In this case the acceptance for forward scattered particles starts at $\sim 5^\circ$. The shielding elements also include cylindrical tungsten absorbers inside the torus bore, a tungsten shield around the FT mounting fixture to the torus, and a lead-tungsten shield downstream of the torus.

One of the main criteria for the shielding design is to maintain an occupancy rate in the drift chambers [11] of less than 4% since higher occupancies adversely affect the track reconstruction efficiency [12]. The drift chamber occupancies were simulated by accumulating hits in the detector elements over 250-ns time frames, which roughly corresponds to the readout time window for the set of drift chambers closest to the beam-target interaction point. The simulated beam was spread out over this time window to match the actual beam structure and was incident on the 5-cm-long LH_2 target such that the design luminosity of 10^{35} cm^{-2} s^{-1} was achieved in the simulation. The simulated target included the aluminum entrance and exit foils and the air gap downstream of the target. The final shielding configuration resulted in occupancies of less than about 3% for the FT-ON configuration and less than about 1.5% for the FT-OFF configuration. Figure 7 shows the origins of background particles hitting the drift chambers for both shielding configurations. The main source of the background is the target, with other sources being the edges of the tungsten shield and the detector enclosures (see figure caption for details).

3. Beamline Monitoring and Performance

During a typical experiment, Hall B shift personnel monitor key beam parameters while beam delivery is controlled by operators in the Machine Control Center. The relevant beamline elements that are used to measure and monitor the key beam parameters are listed in Table 2.

The Synchrotron Light Monitor (SLM) is a photomultiplier tube (PMT) that measures the synchrotron light generated in the last dipole magnet of the 2C beamline that bends the beam into Hall B. The amplitude of the SLM PMT signal is proportional to the beam current and is used to measure the helicity dependence of the beam charge. Due to its dependence on the beam position, it cannot be used as a long term beam current measurement device.

The nano-amp Beam Position Monitors (nA-BPMs) [14] measure the beam current and relative beam position in the transverse, or x-y, plane (z is along the beam direction). The beam position in each direction is measured to an absolute accuracy of 50 μm. The beam current can be measured to an accuracy of $\sim 1\%$ at beam currents above 10 nA, stable over weeks of running. In-

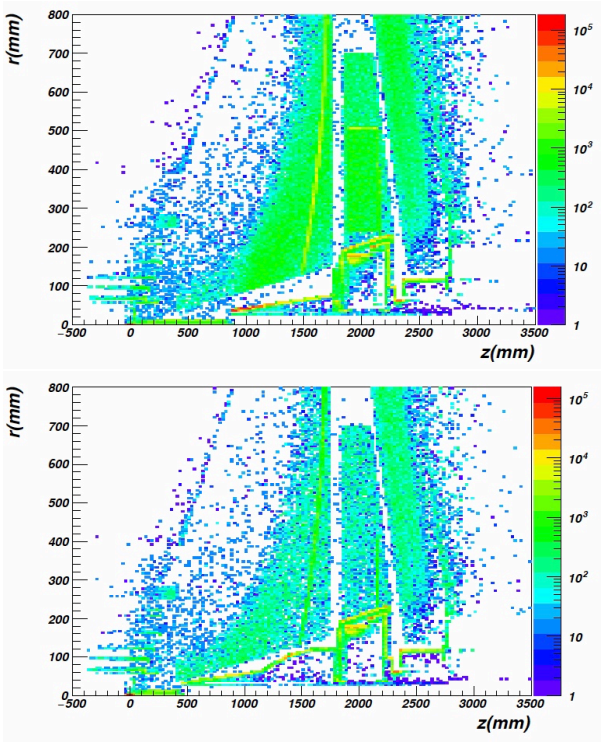

Figure 7: The origin of particles hitting R1 drift chambers (closest to the target) in the r-z plane, where r is the transverse distance from the beam and the z is in the beam direction. The top graph corresponds to the FT-ON configuration and the bottom graph is for FT-OFF. The main source of the background is the target located at $(r, z) = (0, 0)$. The second largest source is the edge of the tungsten shield that starts from (40 mm,850 mm) and extends to (60 mm,1700 mm), followed by the outer edge of the Forward Tagger calorimeter enclosure located around r=200 mm and z=2000 mm. The other large source is the mirror of the High Threshold Cherenkov Counter [13] shown as almost vertical band at around z=1550 mm.

formation from the nA-BPMs can also be used in a feedback loop to keep the beam position fixed.

The wire harps [15] are used to measure the transverse beam profile. These are devices with 25-μm tungsten wires mounted in the horizontal and vertical directions on a support fork that moves the wires into the beam at 45°. As the harp moves into beam, count rates from beam halo counters are combined with the wire position information to determine the beam profile. Since this is an invasive measurement, it is performed primarily during beam setup or when other devices indicate a problem with the beam.

The beam halo counters are PMT-based devices located at various positions along the beamline and are mounted very close to the beam; usually strapped directly to the beam pipe. The PMTs have either scintillating or Cherenkov-light-producing plastic mounted on the photocathode. In addition to providing count rates for the wire harps, these counters are sensitive to any beam halo or undesirable beam interactions. These counters are the main tools to monitor beam-induced background in the hall and, along with the BOM, provide feedback signals for the machine fast shutdown system (FSD). The FSD will stop beam delivery in the case of excessively high background rates in order to protect the detectors.

Table 2: Elements of the Hall B beamline actively monitored and controlled by the experiment shift personnel.

Name and description	Distance from hall center (meters)
Synchrotron Light Monitor	-43.
Wire harp 2C21	-38.8
nA-BPM 2C21A	-37.6
Møller polarimeter	-31.5
nA-BPM 2C24A	-24.5
Wire harp 2C24	-22.0
Upstream halo monitors	-21.7
Hall B tagger dipole	-17.6
Collimator	-15.3
nA-BPM 2H01	-8.0
Wire harp 2H01	-7.4
Midstream halo monitors	-3.9
CLAS12 target	0
Downstream halo monitors	7.5
Beam viewer 2H04	24.0
Dump, Faraday cup	27.0

Other devices that Hall B uses to monitor and measure the beam parameters are the Møller polarimeter located in the upstream tunnel for beam longitudinal polarization measurements, a Faraday cup in the downstream tunnel (electron beam dump) for precise beam current measurements, and a beam viewer that looks at a retractable fluorescent screen installed before the Faraday cup for visual verification of beam transport to the dump.

The Experimental Physics and Industrial Control System (EPICS) [16] is used for monitoring the beam delivery and for control of the beamline devices. Graphical User Interfaces (GUIs) for each application are built using the CS-Studio tools [17]. All variables available in EPICS are archived using the Jefferson Lab MYA data archiver [18]. For continuous monitoring of the beam and the state of the beamline devices, one single GUI was deployed that contains monitored quantities from the beam halo counter rates, magnets, vac-

uum, cryotarget, beam positions and currents, as well as the state of all movable devices. For convenience of monitoring, a timeline of counter rates, along with BPM positions and beam current readings can be displayed separately.

Establishing a production quality electron beam for experiments in Hall B is a two-step process. First, the beam is delivered and tuned in the 2C beamline in the Hall B upstream tunnel. During this tuning process the beam is dumped on the tagger yoke to protect CLAS12 detectors from excessive radiation exposure. The beam profile and transverse position are optimized using the information from the wire harps, the nA-BPMs, and the beam halo counters. Once the 2C beamline is tuned, the beam is then sent to the downstream electron dump and tuned onto the CLAS12 target. The beam is accepted for physics production running when all of the relevant parameters are within expected limits. After production beam has been established, limits on the halo counter rates, beam position, and beam current are set in the CS-Studio alarm system to help Hall B shift personnel monitor the beam quality when running experiments.

3.1. Beam Profile and Position Stability

Establishing and maintaining a high-quality beam is important for obtaining high-quality physics data. Once the beam has been established, scans using the wire harps and nA-BPMs are stored in the MYA archive and are used as reference values over the course of an experimental running period, which may extend over several weeks or months. Figure 8 shows the x– and y–profiles measured with the 2C21 and 2H01 wire harps, located in the upstream tunnel of Hall B and at 7.4 m upstream of the target, respectively. During these measurements, the beam was delivered to the Faraday cup. Figure 9 shows a histogram of the x- and y-widths for sixteen 2H01 harp scans taken over a two month running period. The beam width in both directions fluctuates between 180 μm to 300 μm with an average value of 250 μm.

After the beam has been established for physics running, its position and current stability are continuously monitored using the halo counter rates and the nA-BPMs. Figure 10 shows the distribution of the x– and y–positions about the mean at the 2H01 nA-BPM. The RMS of both distributions is on the order of 20 μm. Such stability is largely due to use of the beam orbit lock system that uses the position readings of the nA-BPMs to drive horizontal and vertical correctors that keep the position of the beam at the set points established at the start of a running period.

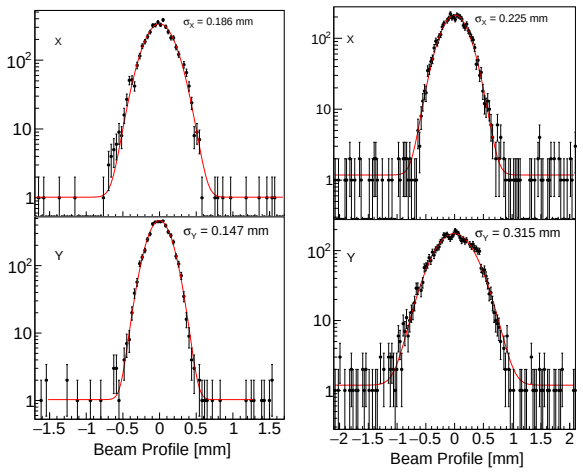

Figure 8: Beam x– (top) and y–profiles (bottom) measured using the wire harp scanners at 2C21 (left) and at 2H01 (right). The red curve is a Gaussian fit with the width shown by the σ values.

3.2. Beam Charge Measurements

An accurate measurement of the total amount of beam charge incident on the target during an experiment is vital for the measurement of experimental cross sections. The Hall B Faraday cup (FC) is the main tool to obtain an accurate *absolute* beam current measurement. A description of the Faraday cup and its readout electronics can be found in Ref. [1]. Since the Faraday cup does not have active cooling, it is limited to 175 W of beam power for long exposures. However, most of the CLAS12 experiments will run with beam currents that exceed the power limit of the FC, thus requiring another method of measuring the beam current. The other devices used to monitor the beam current during the experiment are the nA-BPMs and the SLM, but these devices do not have the long-term stability to provide the accuracy needed over the weeks-long course of an experiment.[1]

Instead, a 5-kW beam dump can be inserted in front of the FC during high-power running. This insertable dump, or beam blocker, is a water-cooled, 28-cm-long copper cylinder (19.5 radiation lengths). While most of the beam is deposited in this beam blocker, the FC still measures a leak-through current that is directly proportional to the total beam current with a very high accuracy of better than 0.5%. In order to use the FC current measurement with the blocker in, a beam-current atten-

[1] The calibration of the nA-BPMs relative to the FC remains stable within a few % for a period of time sufficient for coarse monitoring of the beam current during the experiment.

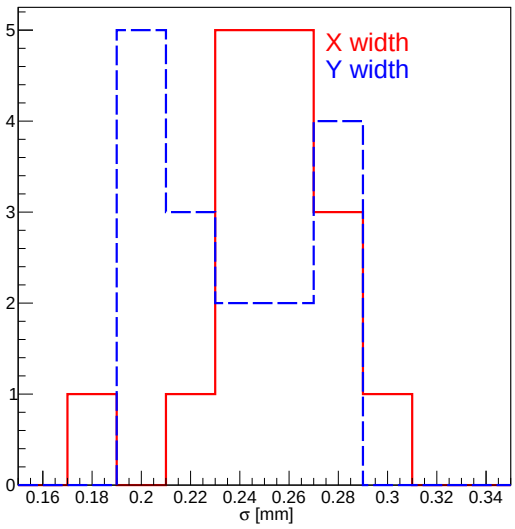

Figure 9: Beam width measured with the 2H01 wire harp over two months of running. The x–width is shown by the solid red histogram and the y–width is shown by the dashed blue histogram.

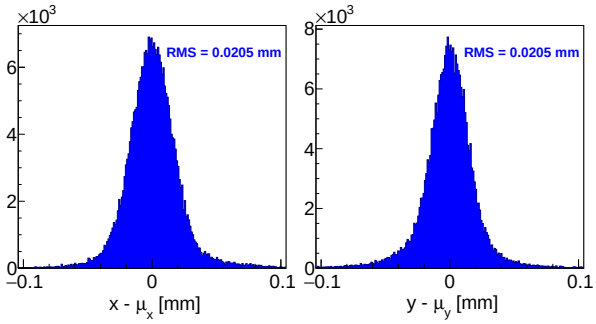

Figure 10: Beam position deviations, $x - \mu_x$ (left) and $y - \mu_y$ (right), over a month of running as measured by the 2H01 nA-BPM.

uation factor, A, must be determined for every beam energy, so that the beam current is given by $I = AI^{in}_{FC}$, where I^{in}_{FC} is the beam current measured at the FC when the beam blocker is in.

To calibrate the attenuation factor, first, a scan of the beam current up to the highest current required by the experiment is done without the beam blocker. The scan is performed rapidly so as to not overheat the FC. These data are used to calibrate the nA-BPM current readings relative to the FC with a calibration factor given by $C = I_{BPM}/I_{FC}$, where I_{BPM} and I_{FC} are the currents measured by the nA-BPM and FC, respectively. The left panel of Fig. 11 shows a distribution of C for a range of beam currents from 15 to 80 nA at a beam energy of 10.67 GeV using the 2C21 nA-BPM. The distribution has a mean of $\langle C \rangle = 1.057$ and Gaussian width of $\sigma_C = 0.0038$, which we use to determine the relative uncertainty in the calibration factor of $\delta C/C = \sigma_C/\langle C \rangle = 0.36\%$.

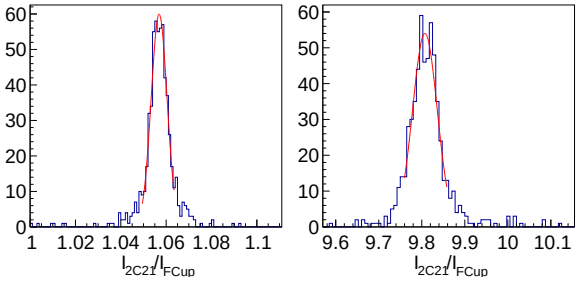

Figure 11: The ratio of beam currents measured by the 2C21 nA-BPM and the Faraday cup without (left) and with (right) the insertable beam blocker. Each distribution has been fit with a Gaussian to obtain the means and widths given in the text.

In the second step, a similar current scan is performed but with the insertable beam blocker in place. Using the now calibrated values of the nA-BPM current reading from the first step, the attenuation factor is given by $A = I^{in}_{BPM}/I^{in}_{FC}$. The distribution of A is shown in the right panel of Fig. 11, which has also been obtained for a range of beam currents from 15 to 80 nA at a beam energy of 10.67 GeV using the 2C21 nA-BPM. The distribution has a mean of $\langle A \rangle = 9.807$ and a Gaussian width of $\sigma_A = 0.0306$, which leads to a relative uncertainty of $\delta A/A = \sigma_A/\langle A \rangle = 0.31\%$. Combining the uncertainties from the calibration of the nA-BPMs and the attenuation factor leads to a total relative uncertainty in the blocker-in FC current measurement of $\delta I_{FC}/I = 0.48\%$.

A simultaneous measurement of the attenuation factor has been done using the 2C24 nA-BPM resulting in $\langle A \rangle = 9.809$, which agrees well with the 2C21 nA-BPM measurement. More details of this calibration can be found in Ref. [19]. Results obtained for other energies are shown in Table 3 with details found in Ref. [20].

Bean energy (GeV)	FC Attenuation
6.4	16.28
6.6	16.24
7.54	14.90
10.2	9.96
10.67	9.81

Table 3: FC attenuation factors for different beam energies. The estimated relative uncertainty of the attenuation factor is < 0.5%.

4. Møller Polarimeter

The determination of the electron beam polarization is done in Hall B using a coincidence Møller polarimeter. The polarimeter is based on $\vec{e} + \vec{e} \rightarrow e + e$ elastic scattering (Møller scattering). A detailed description of Møller scattering is presented in Ref. [21].

For a longitudinally polarized electron beam incident on a longitudinally polarized electron target, the center-of-momentum (CM) frame cross section is given by [22, 23]

$$\frac{d\sigma}{d\Omega} = \frac{d\sigma_0}{d\Omega}\left(1 + P_B A_{zz} P_T\right), \tag{1}$$

where $d\sigma_0/d\Omega$ is the unpolarized cross section, P_B and P_T are the longitudinal components of the beam and target polarization, respectively, and A_{zz} is the analyzing power. The unpolarized cross section and analyzing power can be precisely calculated through quantum electrodynamics, which gives

$$\frac{d\sigma_0}{d\Omega} = \left(\frac{\alpha\left(3 + \cos^2\theta_{CM}\right)}{2m_e\gamma\sin^2\theta_{cm}}\right)^2, \tag{2}$$

and

$$A_{zz} = -\frac{(7 + \cos\theta_{CM})\sin^2\theta_{CM}}{\left(3 + \cos^2\theta_{CM}\right)^2}, \tag{3}$$

where α is the fine structure constant, θ_{CM} is the CM polar scattering angle, m_e is the electron mass, and $\gamma = \sqrt{(E + m_e)/2m_e}$ with E the lab energy of the incident electron. From the above formulas, one sees that A_{zz} has a maximum magnitude of 7/9 at $\theta_{CM} = 90°$, which is the central scattering angle for our polarimeter.

Forming the beam-helicity-dependent asymmetry gives

$$A = \frac{\frac{d\sigma}{d\Omega}_+ - \frac{d\sigma}{d\Omega}_-}{\frac{d\sigma}{d\Omega}_+ + \frac{d\sigma}{d\Omega}_-} = A_{zz}\left(\theta_{CM}\right) P_B^z P_T^z, \tag{4}$$

where the ± refers to cases where the beam helicity and the target polarization are aligned or anti-aligned. The asymmetry can be measured from the yields according to

$$A = \frac{N_+ - N_-}{N_+ + N_-} = \langle A_{zz}\rangle P_B^z P_T^z, \tag{5}$$

where $\langle A_{zz}\rangle$ is the effective analyzing power corrected for the finite-angle acceptance of the polarimeter and atomic-electron motion (also known as the Levchuk effect [24]).

The CLAS12 Møller polarimeter detects the scattered electrons in coincidence near $\theta_{CM} = 90°$, the peak of A_{zz}. The coincidence method has the advantage, as compared to single-arm Møller polarimetry, of producing a clean data set without having to do energy-dependent background subtractions (see, for example Ref. [25]). Accidental background rates are typically less than 10% of the real coincident rate for our polarimeter. The accidental rate is measured and included as a correction.

4.1. Polarimeter Design

The layout for the polarimeter is shown in Fig. 12. The essential elements of the polarimeter include a polarized target system, a pair of quadrupole magnets both operated in a dispersive mode to separate the scattered electrons from the unscattered beam electrons, a pair of detectors, and lead shielding between the second quadrupole and the detectors to reduce background. The detectors consist of scintillating fibers packed with lead powder to form a 15.6-cm wide, 9.0-cm high, and 25-cm deep block with a light guide and are read out with a PMT. The detectors are surrounded by lead bricks with a scattered-particle aperture of 7.62 cm in the horizontal direction and 5.0 cm in the vertical direction. The locations of the quadrupoles and detectors along with the quadrupole fields were determined by simulations of the layout. The locations and fields were adjusted in the simulation so that $\theta_{CM} = 90° \pm (4° - 4.5°)$.

4.1.1. Polarimeter Target

The target system has a pair of 25-μm-thick permendur foils on a remotely controlled insertion table housed in a vacuum chamber, as shown in Fig. 13. Permendur is an iron-cobalt alloy (49% Fe, 49% Co, 2% Va) that has a maximum saturated polarization of approximately 8% along the plane of the foil when subjected to a magnetic field of greater than about 40 G. To create a longitudinally polarized target, the plane of the foil is oriented at ±20° relative to the beamline and subjected to a longitudinal magnetic holding field produced by a pair of Helmholtz coils on either side of the target chamber. Since only the longitudinal component of the polarization contributes to the measured asymmetry, the target polarization used in Eq. 5 is $P_T^z = P_T \cos 20°$. The 20° tilt angle of the target maximizes the longitudinal component of the polarization, while keeping the mounting hardware out of the beam.

The polarization of the permendur target is related to the magnetization, M, of the foil by [26]

$$P_T = M\left(4.546 \times 10^{-5} \pm 2.9 \times 10^{-7}\right), \tag{6}$$

where M is measured in units of G. The foil magnetization is measured in a separate setup consisting of a

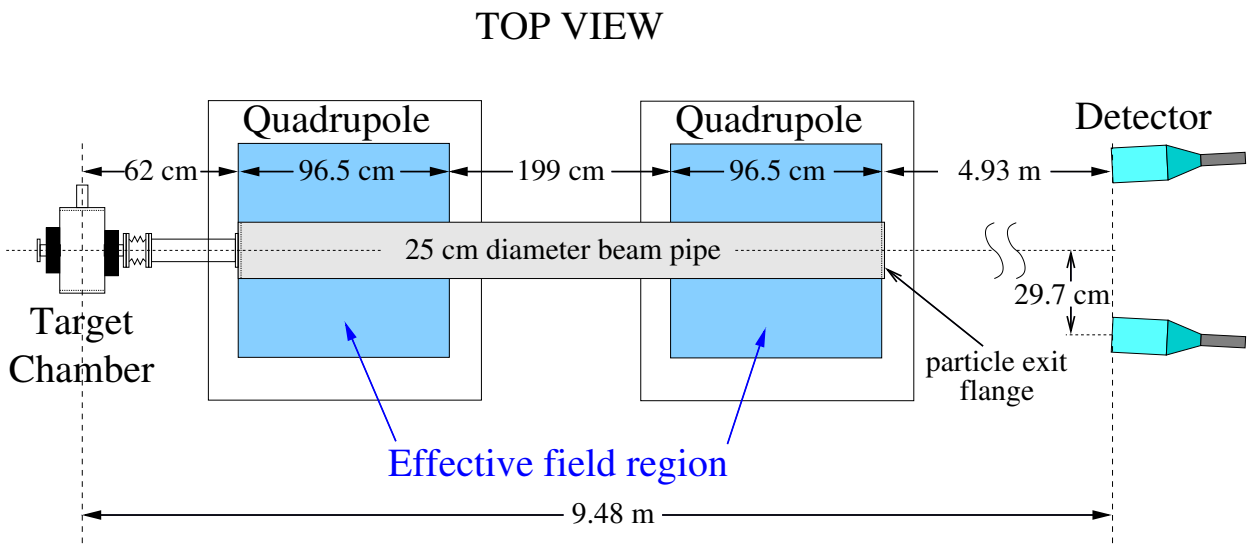

Figure 12: Layout of the CLAS12 Møller polarimeter. The detector shielding is not shown.

solenoid coil used to produce the magnetizing field, H, into which the target foil is placed and a pickup coil that is located at the center of the foil. A fixed current is applied to the solenoid to polarize the target. The direction of the current is then flipped over a time period of ~0.15 s leading to an induced voltage across the pickup coil. A typical pickup-coil signal is shown in Fig. 14, which was measured with a digital oscilloscope. The flat part of this signal (highlighted by the black constant fit) corresponds to the changing applied field while the narrow peak in the middle of the signal results from the change in the target foil magnetization. Applying Faraday's law to the flat part of the signal (using the fit to interpolate under the peak) yields

$$\int_H V dt = 2HN_T\langle A_{\rm coil}\rangle \rightarrow H = \frac{\int_H V dt}{2N_T\langle A_{\rm coil}\rangle}, \qquad (7)$$

where $\int_H V dt$ is the area under the pickup coil signal excluding the peak, N_T is the number of turns in the pickup coil, and $\langle A_{\rm coil}\rangle$ is the average cross-sectional area of the pickup coil.

The target polarization is related to the difference between the total area, $\int_{\rm total} V dt$, of Fig. 14 and the area leading to H and is given by [26]

$$P_T = (1.474 \pm 0.010)\, l \frac{\left(\int_{\rm total} V dt - \int_H V dt\right)}{mN_T}, \qquad (8)$$

where l is length of the target in cm, m is the mass of the target in grams, and both areas are measured mVs.

Figure 15 shows a typical saturation curve for the target, i.e. how the target polarization depends on the applied field. Measurements were done with two different pickup coils with the difference between the two results indicating the systematic uncertainty associated with knowledge of the pickup coil geometry. For this foil, the polarization saturated at a value of $P_T = 6.17 \pm 0.047\%$, where the uncertainty is a combination of the statistical uncertainties from the linear fits of the saturation region of the curves and the variation between the two measurements. Additional uncertainties associated with the leading factor in Eq. 8, the other measured quantities in Eq. 8, estimated variations in the target material thickness, and the uncertainty in the target angle relative to the beam leads to a total relative uncertainty $\delta P_T^z / P_T^z = 0.014$.

4.2. Analyzing Power Corrections and Uncertainties

Simulations have been performed to estimate effects due to atomic motion of the electrons and to estimate uncertainties associated with the polarimeter geometry. The simulation begins by randomly selecting the scattering angles θ_{CM} and ϕ_{CM} and then transporting the scattered electrons through the magnets and toward the detectors. For events in which both electrons hit the detectors, we determine an average analyzing power, $\langle A_{zz}\rangle$. The motion of the atomic electrons has been included in the simulation according to Ref. [24]. Figure 16 shows $\langle A_{zz}\rangle$ as a function of beam energy both with and without atomic-electron motion included in the simulation. The lower curve includes the motion

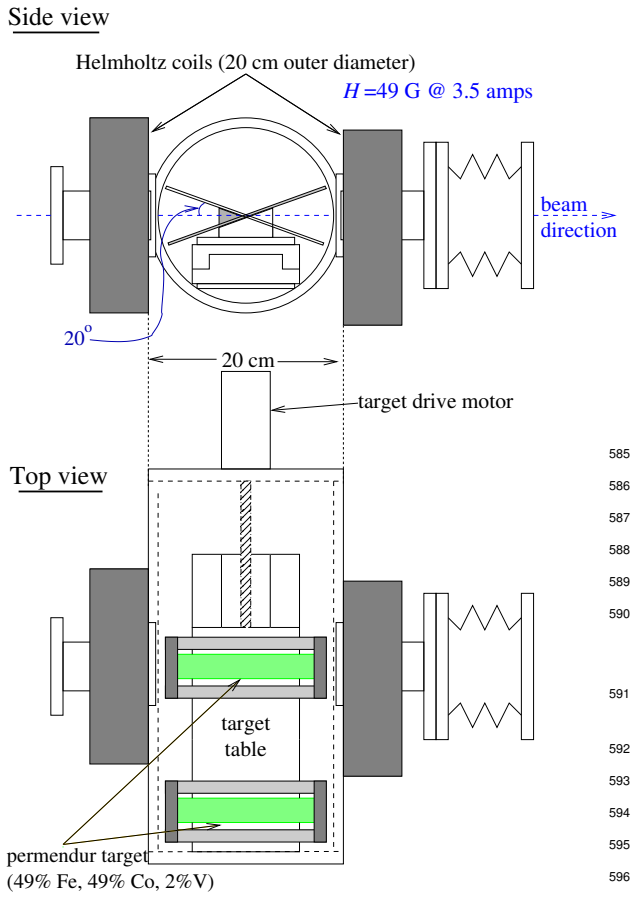

Figure 13: Side and top view layouts of the CLAS12 Møller polarimeter target chamber shown with the beam-left target inserted.

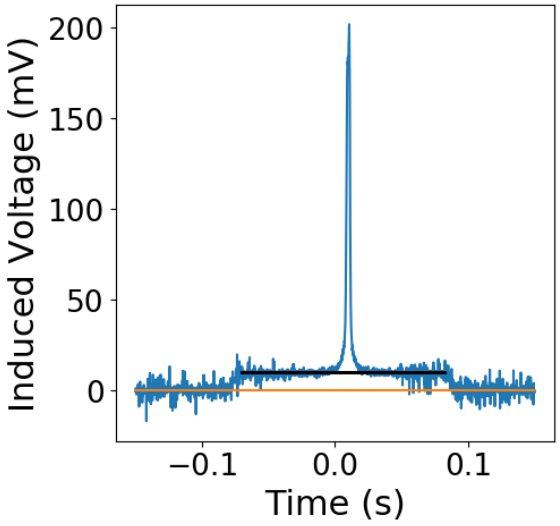

Figure 14: Target pickup coil signal showing the induced voltage as a function of time. The flat part of the signal (fit with black line) corresponds to the changing applied Helmholtz field, H, while the sharp peak near the middle corresponds to the flip in the target magnetization.

effect and is fit with the functional $\langle A_{zz} \rangle = -0.777123 + (2.9249 \times 10^{-3})/E$. The estimated relative uncertainty is $< 0.01\%$ and was determined by looking at variations in $\langle A_{zz} \rangle$ for reasonable variations in the geometry (locations of quadrupoles and detectors) and magnetic fields.

4.3. Beam Polarization Measurements

Beam polarization measurements are usually done on a weekly basis or after changes to the accelerator configuration. The shift personnel use what is in essence a push-button GUI interface. The user selects which target to use (left or right) and the Helmholtz coil polarity. The settings for the quadrupoles are automatically calculated based upon the beam energy. Individual Møller runs are usually done for both targets with a statistical precision of $\pm 1.5\%$, which is slightly smaller than the total systematic uncertainty. The underlying software calculates the beam polarization using the beam-helicity-gated true and accidental coincidence rates from the Møller detectors along with the beam-helicity related charge asymmetry measured using the SLM. At the end of a Møller run the beam polarization is stored in the GUI and goes automatically to the electronic logbook. The scaler readouts during the run are stored in the run file while the polarization measurement is stored in the database.

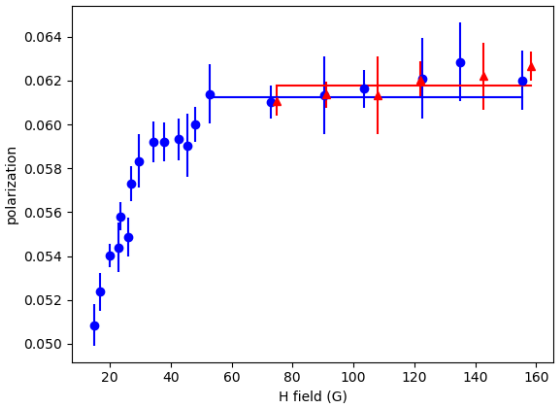

Figure 15: Target polarization vs. applied magnetic field, H, measured with two different pickup coils. A constant fit to the flat part of the curves yields values of 6.18 ± 0.03% for coil 1 (red diamonds) and 6.15 ± 0.04% for coil 2 (blue dots), where the uncertainties are statistical only.

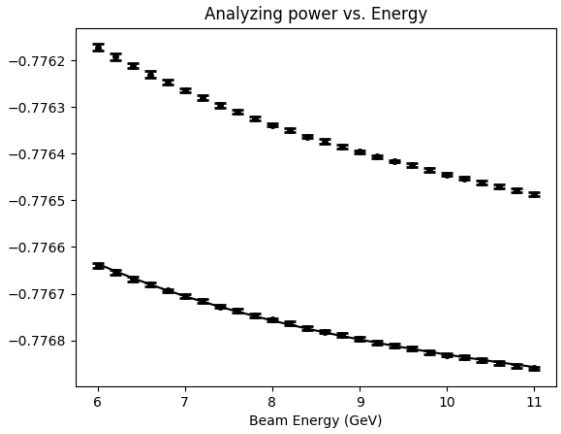

Figure 16: Average analyzing power $\langle A_{zz} \rangle$ as a function of beam energy from simulation. The upper/lower points exclude/include motion of the atomic electrons. The error bars are statistical only. The curve on the lower points is a fit discussed in the text.

The results of the beam polarization measurements taken during the fall 2018 run period are shown in Fig. 17. There are two distinct regions of beam polarization with average polarizations of 85.95 ± 1.29% and 89.22 ± 2.51%. These two regions differ by settings of the angle, θ_W, of the Wien filter in the injector. The initial Wien-filter angle was set to maximize the beam polarization in Hall B and was based on a calculation of the electron spin precession in the accelerator. However, the polarization in the early part of the running period fell below the expected maximum of about 90%, which was measured at the injector by a Mott polarimeter, indicating an incorrectly calculated θ_W. In order to find the optimum value of θ_W, two more Møller measurements of the beam polarization in Hall B were performed at $\theta_W = 25°$ and 70°. The result of these measurements along with the average at $\theta_W = 50°$ are shown in Fig. 18. Fitting these three points with a function of $a \cos(\theta_W - b)$ (dashed curve), where a and b are fit parameters, shows that the maximum polarization of about 90% in Hall B occurs for $\theta_W \approx 40°$.

Figure 17 has two sets of Hall B polarimeter measurements done with and without a half-wave plate. The half-wave plate rotates the electron spin by 180°. The measurements with and without the the half-wave plate agree within statistical uncertainties.

5. Summary

The first CLAS12 experiment in 2018 took data successfully at three beam energies; 10.6 GeV, 6.4 GeV, and 2.2 GeV with a liquid-hydrogen target. High quality beam was delivered with a beam size of < 200 μm and a beam halo as small as 10^{-4} at 5σ away from the core. The beam position was maintained within ~200 μm throughout the run by the beam feedback system and the fast shutdown system worked in protecting the CLAS12 detectors from errant beam exposure. With typical Møller polarimeter runs, the beam polarization can be measured to an absolute precision of ~2.5%.

6. Acknowledgements

The authors are grateful for the outstanding efforts by the staff of the Accelerator Division and the Hall B Engineering Group at Jefferson Lab during the installation and running of the experiment. We also thank the CLAS12 Collaboration for manning shifts and taking high quality data. This material is based upon work supported by the U.S. Department of Energy, Office of Science, Office of Nuclear Physics under contract DE-AC05-06OR23177 and by the Italian Instituto Nazionale di Fisica Nucleare.

[1] B. A. Mecking *et al.*, The CEBAF Large Acceptance Spectrometer (CLAS), Nucl. Instrum. and Meth. A **503**, 513 (2003). doi:10.1016/S0168-9002(03)01001-5.

[2] HPS update to PAC39, https://www.jlab.org/exp_prog/proposals/12/C12-11-006.pdf.

[3] N. Baltzell *et al.*, The Heavy Photon Search Beamline and its Performance, Nucl. Instrum. and Meth. A **859**, 69 (2017). arXiv:1612.07821, doi:10.1016/j.nima.2017.03.061.

[4] D. I. Sober *et al.*, The Bremsstrahlung Tagged Photon Beam in Hall B at JLab, Nucl. Instrum. and Meth. A **440**, 263 (2000). doi:10.1016/S0168-9002(99)00784-6.

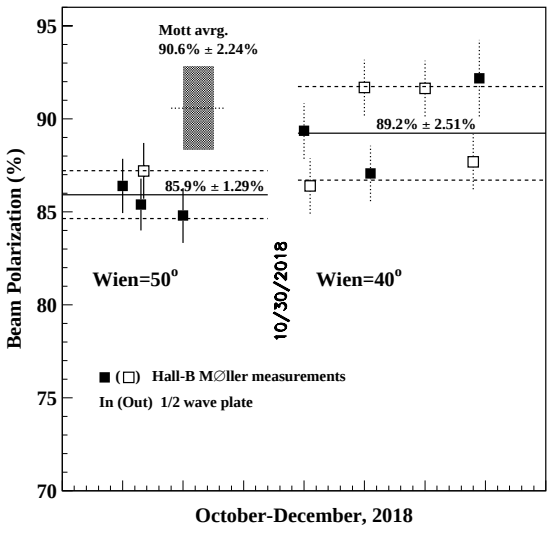

Figure 17: Beam polarization measured in Hall B during the fall 2018 running period. Prior to October 30 the measurements from the Hall B polarimeter (squares) averaged to 85.9% ± 1.2% (stat.), which is lower than the expected 90% from the injector Mott measurements (black band). After optimizing the Wien-filter angle the average polarization measured in Hall B was measured to be 89.2% ± 2.5% (stat.). The filled and open symbols correspond to measurements made with and without a half-wave plate, respectively. Error bars are statistical only.

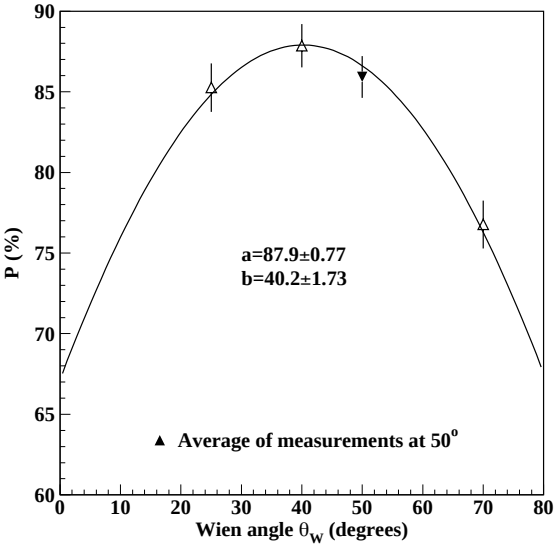

Figure 18: Beam polarization measurements at different Wien angle settings taken during the fall 2018 run period. The dashed curve is the cosine-function fit to the data points. The filled point is the average over all measurements with the angle set to 50° and the open points are from single measurements. Error bars are statistical only.

[5] T. T. Bohlen, F. Cerutti, M. P. W. Chin, A. Fassò, A. Ferrari, P. G. Ortega, A. Mairani, P. R. Sala, G. Smirnov, V. Vlachoudis, The FLUKA Code: Developments and Challenges for High Energy and Medical Applications, Nucl. Data Sheets **120**, 211 (2014). doi:10.1016/j.nds.2014.07.049.

[6] https://www.ansys.com/-/media/Ansys/corporate/resourcelibrary/brochure/ansyscapabilities180.pdf.

[7] C. Keith, Polarized Solid Targets at Jefferson Lab, PoS PSTP2015, 013 (2015). doi:10.22323/1.243.0013.

[8] M. A. Antonioli *et al.*, The CLAS12 Silicon Vertex Tracker, to be published in Nucl. Inst. and Meth. A, (2020). (see this issue)

[9] M. Ungaro *et al.*, The CLAS12 Geant4 Simulation, to be published in Nucl. Inst. and Meth. A, (2020). (see this issue)

[10] M. Battaglieri *et al.*, The CLAS12 Forward Tagger, to be published in Nucl. Inst. and Meth. A, (2020). (see this issue)

[11] M.D. Mestayer *et al.*, The CLAS12 Drift Chamber System, to be published in Nucl. Inst. and Meth. A, (2020). (see this issue)

[12] V. Ziegler *et al.*, The CLAS12 Software Framework and Event Reconstruction, to be published in Nucl. Inst. and Meth. A, (2020). (see this issue)

[13] Y. Sharabian *et al.*, The CLAS12 High Threshold Cherenkov Counter, to be published in Nucl. Inst. and Meth. A, (2020). (see this issue)

[14] R. Ursic, M. Piller, R. Flood, E. Strong, and L. Turlington, 1 nA Beam Position Monitoring System, Conf. Proc. C970512, 2131 (1997).

[15] M. McCaughan, M. Tiefenback, and D. Turner, Improvements to Existing Jefferson Lab Wire Scanners, in: Proceedings, 4th International Particle Accelerator Conference (IPAC 2013): Shanghai, China, May 12-17, 2013, 2013, p. MOPWA076. URL http://JACoW.org/IPAC2013/papers/mopwa076.pdf

[16] https://epics-controls.org.

[17] http://controlsystemstudio.org.

[18] C. Slominski, https://wiki.jlab.org/lerf/images/7/75/Archive_user.pdf.

[19] R. Paremuzyan and S. Stepanyan, CLAS12-Note 2018-003, (2018). URL https://misportal.jlab.org/mis/physics/clas12/viewFile.cfm/2018-004.pdf?documentId=58

[20] R. Paremuzyan and S. Stepanyan, CLAS12-Note 2018-004, (2018). URL https://misportal.jlab.org/mis/physics/clas12/viewFile.cfm/2018-003.7gev.pdf?documentId=57

[21] B. Wagner, H. G. Andresen, K. H. Steffens, W. Hartmann, W. Heil, and E. Reichert, A Møller Polarimeter for CW and Pulsed Intermediate-Energy Electron Beams, Nucl. Instrum. and Meth. A **294**, 541 (1990). doi:10.1016/0168-9002(90)90296-I.

[22] C. Møller, Ann. Phys. **14**, 531 (1932).

[23] A. A. Kresnin and L. N. Rosentsveig, J. Exp. Theor. Phys. (USSR) **32**, 353 (1957).

[24] L. G. Levchuk, The Intraatomic Motion of Bound Electrons as a Possible Source of a Systematic Error in Electron Beam Polarization Measurements by Means of a Møller Polarimeter, Nucl. Instrum. and Meth. A **345**, 496 (1994). doi:10.1016/0168-9002(94)90505-3.

[25] J. Arrington, E. J. Beise, B. W. Filippone, T. G. O'Neill, W. R.

Dodge, G. W. Dodson, K. A. Dow, and J. D. Zumbro, A Variable Energy Møller Polarimeter at the MIT-Bates Linear Accelerator Center, Nucl. Instrum. and Meth. A **311**, 39 (1992). doi:10.1016/0168-9002(92)90849-Y.

[26] H. R. Band, G. Mitchell, R. Prepost, and T. Wright, A Møller Polarimeter for High-Energy Electron Beams, Nucl. Instrum. and Meth. A **400**, 24 (1997). doi:10.1016/S0168-9002(97)00984-4.